Chapter 8
Development of New Lagrangian Computational Methods for Ice-Ship Interaction Problems: NICESHIP Project

Julio García-Espinosa, Eugenio Oñate, Borja Serván Camas, Miguel Angel Celigueta, Salva Latorre and Jonathan Colom-Cobb

Abstract This document presents the activities carried out to date (04/2019) in the project 'Development of new Lagrangian computational methods for ice-ship interaction problems' (NICE-SHIP). The NICE-SHIP project aims at developing a new generation of computational methods, based on the integration of innovative Lagrangian particle-based and finite element procedures for the analysis of the operation of a vessel in an iced sea, taking into account the different possible conditions of the ice. It is expected that the computational analysis techniques to be developed in NICE-SHIP will allow ice-class vessel designers to accurately evaluate the loads acting on the structure of a ship navigating in iced-seas and, in particular, to determine the ice resistance of the ship in different ice conditions.

J. García-Espinosa (✉)
CIMNE MARINE. C/ Pla del Palau, 18, FNB (BarcelonaTech), 08003 Barcelona, Spain
e-mail: julio@cimne.upc.edu

E. Oñate · M. A. Celigueta · S. Latorre
CIMNE, Barcelona, c/Jordi Girona s/n Campus Nord UPC, Edifici C1, 08034 Barcelona, Spain
e-mail: onate@cimne.upc.edu

M. A. Celigueta
e-mail: maceli@cimne.upc.edu

S. Latorre
e-mail: latorre@cimne.upc.edu

E. Oñate · M. A. Celigueta · S. Latorre
Universitat Politecnica de Catalunya - BarcelonaTech, Barcelona, Spain

B. S. Camas · J. Colom-Cobb
CIMNE MARINE, c/Escar 6-8, Edificio NT3 FNB, 08039 Barcelona, Spain
e-mail: bservan@cimne.upc.edu

J. Colom-Cobb
e-mail: jcolom@cimne.upc.edu

8.1 Introduction

8.1.1 Navigation in the Arctic Area

The Arctic region is taking up more and more room within the international agenda. The main reason is the vast reservoirs of oil, gas, minerals, fresh water, fishing, etc. In parallel, the increase of the average temperature in arctic regions is boosting the ice setback, which allows keeping the arctic navigation routes open for longer periods, open new ones, and expand the commercial fishing. In fact, shipping lines are more and more enthusiastic about the potential that these new routes offer, given the save of time and energy cost that might offer compared to longer traditional routes. Just like the New York Times reported in 2017 in its chronicle "As Arctic Ice Vanishes, New Shipping Routes Open", the exploitation of the arctic routes is becoming more and more real every day. No one doubts that the commercial activity in the Arctic is going to grow substantially in the following years. Northern routes can save up to 30% in time and fuel consumption, as well as the corresponding emission of contaminants. As an example, the well-known Northern Sea Route (NSR) that connects Europe with Eastern Asia is 7000 km shorter than the traditional route through the Suez Channel (see Fig. 8.1).

Based on several studies (Nadukandi et al. [22]) the present fleet of ships suitable to navigate in arctic areas is old and insufficient. Then the future growth of the Arctic
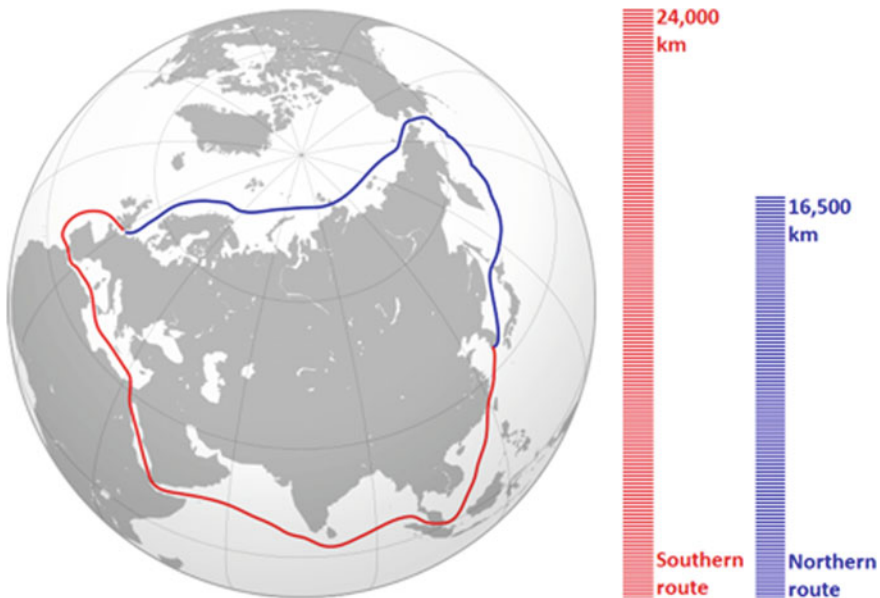
Fig. 8.1 Northern Sea Route versus Southern Sea Route. Source: Wikimedia Commons

traffic will stimulate undoubtedly the demand of icebreakers and ships reinforced for ice navigation and in the long term will create a scenario of big opportunities for the European ship building industry. In fact, the growing interest in the opportunities offered by the Arctic routes has motivated a number of projects to design a new generation of large merchant vessels capable of breaking ice and open their way through it, as well as offshore platforms for oil and gas extraction (Nadukandi et al. [22]; Shipyards' and Maritime Equipment Association (SeaEurope) [25]). Large shipping companies, like Maersk, are positioning themselves to exploit the NSR. In fact, in 2018 the Venta Maerks will become the first large container ship to navigate through the NSR in order to acquire data and analyse the viability to commercially exploit this route in a near future.

The potential grow of the maritime traffic in the Arctic routes has generated a deep concern among environmentalists, and the response of the international community has been the adoption of the international code for ships operating in polar waters ("Polar Code") by the International Maritime Organization (IMO). The Polar Code became effective on January 1st 2017 with the corresponding amendments within the international agreement "Safety Life at Sea" (SOLAS) and the "International Convention for the Prevention of Pollutions from Ships" (MARPOL), so that the "Polar Code" becomes mandatory. This code includes regulations regarding safety and pollution for ships operating in arctic routes.

8.1.2 The Design of Ships for Navigation in Ice

The propulsion systems and hulls of ice class vessels have been, up to date, designed and built based on the experience accumulated by navigating the Northern Sea. The first icebreakers designs tested in model basin appeared in the 60s (Corlett and Snaith [7]). These designs were launched also in the 60s, and they were required to integrate at the bow a bulb with cutting shapes of small penetration angles, so that it will cut through the ice shells easily. The power required by the propulsive system was more than double the required for navigation in open waters.

Current icebreakers clear the way by pushing the ice shells. Since the bending strength of the ice shells is so low, these break with no much change in the ship velocity and pitch. In case of thick ice, the icebreaker bow can get onto the ice, using the ship weight to break it under the ship along its pass. The channel opened by the icebreaker is used by a convoy that navigate among the broken ice blocks (brash ice). These ships must be designed for this kind of navigation in brash ice (see Fig. 8.2).

The full interaction between the ice and the hull of the ship makes quite difficult the design of these ice class ships. An important objective in the design of an icebreaker is to minimize the energy required to break down and submerge the ice blocks. The added resistance due to the ice is currently estimated using analytic methods based on regression using experimental data obtained from full and model scale. Unfortunately, due to the complexity of the problem, this precision of these estimations is quite poor. Therefore, model testing in ice tanks is necessary in order to obtain a more precise estimation under different scenarios. Independently of the

Fig. 8.2 Icebreaker clearing the way for a container ship. Source: Wikimedia Commons

method used, the performance of the new icebreakers is finally verified in sea trials with the actual ship. The accumulation of ice blocks can significantly increase the ship drag. Hence, ice class ships have a hull designed to steer the ice blocks around or under the hull, leading to a risk of collision with different elements such as the propeller, shafts, rudders… This capability to steer the ice blocks away from these elements is critical.

In the last decades, a number of studies have been carried out in different model basins to evaluate new hull designs in terms of efficiency and safety (Kashteljan et al. [18]; Lewis and Edwards J [20]). With the appearance of vast natural resources in the Arctic regions, these studies are being extended to analyse ships capable of extracting those resources and operating in the polar regions, as well as breaking the ice to clear the way.

8.1.3 History and State of the Art in Simulation and Analysis of Ship Navigation in Ice

Since the 60s several authors have tried in developing formulations capable of estimating the ship resistance in icy waters. For instance, (Kashteljan et al. [18]) presents the first empirical formula to estimate the resistance that accounts for ice at the water

surface in both states, compact and broken. In 1970, (Lewis and Edwards Jr [20]) deducted an equation to determine the resistance of icebreakers, compared the results with real data, and afterwards calibrated their formula for a better match. In recent works (Cho and Lee [4]; Cho et al. [6]) different formulations have been presented to analysed different resistance components, using multiple regression methods to adjust the results to those obtained experimentally using ship models. Nevertheless, the prediction capability of all these formulations is very limited due to the large dependence on the specific ice properties. In terms of numerical simulation, a number of works have been published in the last years modelling the ship as a rigid body with just three degrees of freedom (Hu and Zhou [12]; Su et al. [26]; Zhou et al. [27]). These numerical models take into account the immersion, breaking, and accumulation of ice by means of simplifies empirical formulas. In addition, we can find works using commercial simulation tools to simulate the ship interacting with ice blocks (Kim et al. [19]; Cho et al. [5]). A lot of effort has been put into the above mentioned works in validating the predicted results against experimental data obtained in model basins. However, there is still a long way to develop a model able to accurately predict the actual interaction among the ship, the ice, and the water dynamics due to the simplifications used in the above mentioned formulations.

Looking at navigating surrounded by ice blocks (brash ice), it is obvious that we are in front of a very complex problem. It consists of a multiphase flow (ice and water), where the solid phase (ice) is randomly distributed in blocks all over the domain under study. Nowadays, most available models to solve multiphase flows are not suitable since they are based on an interface capturing scheme and solving one fluid with properties suddenly changing across the interface (Garcia-Espinosa et al. [11]). In general, these methods introduced numerical erosion in the interface capturing scheme leading to a change of shapes of the solid phases (Idelsohn et al. [16]). An alternative to these methods is the interface tracking methods, which use a Lagrangian approach to evolve the interface and provide higher precision (Idelsohn et al. [14]; Onate et al. [23]). However, most of these methods are conceived to analyse a limited number of phases and cannot consider the complex interaction among the ice blocks, the ship and its appendages. The limitations found in the aforementioned methods is one of the main motivations of the NICE-SHIP project, which main objective is the theoretical development and implementation of a new generation of Lagrangian computational methods for the analysis of the operation of a vessel in an iced sea, taking into account the different possible conditions of the ice. In the following sections, the activities carried out to date (04/2019) in the development of the above-mentioned Lagrangian computational methods are presented.

8.2 NICE-SHIP Project Scenarios

In order to organize effectively the tasks of the project and focussing on a practical approach, the work of the development team in the NICE-SHIP project has been focused on the study of two specific scenarios. The first scenario is the icebreaking of ships in flat surfaces of floating ice of different thicknesses. The goal of this analysis

scenario is to validate the constitutive models developed for flat ice analysis, as well as the contact and friction forces models between ship and ice. For this purpose, a constitutive material model in the context of the Discrete Element Method (DEM) has been developed. The model developed to analyse the first scenario will be useful to analyse the icebreaking performance and added resistance of ships in level ice. The second scenario to be studied is the navigation of ships in brash ice (and broken ice). Brash ice is made of accumulations of floating ice made up of fragments not more than 2 m across. A FEM semi-Lagrangian fluid-dynamics solver (SL-PFEM) fluid dynamics model has been selected to analyse this scenario. This model will be able to simulate the evolution of the ice around or under the vessel. SL-PFEM solver will be based on the correction of the momentum equation of the fluid-dynamics solver by adding the drag force generated by the ice debris packets. Possible breaking of the larger ice fragments will be ignored in this scenario. This model will be useful to analyse the ice navigation performance of ships and ice-appendages interaction phenomena.

8.2.1 Scenario 1: Analysis of the Icebreaking Performance of Ships in Level Ice

8.2.1.1 Introduction to the Discrete Element Method (DEM)

The Discrete Element Method (henceforth DEM) was born in 1971 when Cundall introduced it for the first time the International Society of Rock Mechanics (Cundall [8]). Afterwards, Cundall and Strack applied it to fracture mechanics and solids (Lu et al. [21]). The DEM is a numerical tool thought to simulate the mechanical behavior of a system formed by a set of separate elements (particles) arbitrarily configured. Each particle is defined as a discrete element that forms part of the whole system and has an independent movement. The interaction with other particles is due to contacts and the overall behavior of the system is described by the cohesive (frictional) contact laws.

From the beginning of the DEM, it has been extensively used as a numerical technique for reproducing the behavior of granular materials (non-continuum media) with very good results. However, in recent years the DEM has also been extended to the continuum media. Intense research has been carried out on multi-fracture and failure of solids involving geomaterials (soils, rocks and concrete) (Onate et al. [24]). Even more recently, the DEM has been used on modelling the mechanical behavior of ice, considered a frictional material (Lu et al. [21]; Di et al. [9]; Ji et al. [17]). The material in the DEM is typically represented as a collection of rigid particles (spheres in 3D and discs in two 2D) interacting among themselves at the contact interfaces in the normal and tangential directions. Material deformation is assumed to be concentrated at the contact points. Appropriate contact laws are defined in order to obtain the desired macroscopic material properties.

The continuum modelling using the DEM is relatively new. The fracture behavior of solids (concrete, rocks, ice, ceramics) and other brittle materials, when loaded under severe ratios, has become an area of intense research. The DEM is appropriate for reproducing the transition of some materials from continuum to non-continuum scenarios. At the first stage, the whole analyzed system is considered as a continuum configured by a package of discrete elements. Afterwards, when it is loaded under certain conditions, the main system is divided into smaller groups of single or several particles. When modelling the continuum media with the DEM, any continuum contact between two neighbouring particles must be understood as a spring linking their centers that is in equilibrium when the two particles are tangentially in contact. Thereby, as they get closer the spring will be shortened and so repulsive forces will appear. On the other hand, if they get farther the attraction forces of the spring will keep them together. Furthermore, the damping force will always be acting as long as the contact has not failed. The transition from the continuum to the non-continuum scenarios is produced when a contact fails. Once the bonds are broken, the affected particles begin to act in the same way as in the non-continuum case. The contact between two neighbouring particles is then modelled by the linear-spring-dashpot model, which originate forces when there is overlap between two neighboring particles. Thus, the interaction phase in the non-continuum media only occurs when at least two particles are in contact. The ability of the bonded DEM (with some breakage criteria) to reproduce multi-cracking phenomena in strongly cohesive materials is one of the main reasons why the DEM has been chosen to analyse this scenario.

Depending on the application of interest, many thousands or even millions of particles may be required to describe the overall analyzed system. Furthermore, the simulations may consist of up to millions of time steps. This clearly shows the limitations of the DEM, which are mainly related with computational demand aspects.

8.2.1.2 Contact Interface

Assuming that an individual particle is connected to the adjacent ones by appropriate relationships at the contact interfaces, these relationships define either a perfectly bond or a frictional sliding situation at the interface. Particles are assumed to be spherical and can have very different sizes. Each particle i is characterized by the sphere of radius r_i. We will assume that particles i and j are in contact at a point c located at a distance $(1 + \beta)r_i$ or $(1 + \beta)r_j$ from the centres of particles i and j, respectively, where β is a positive number, typically $0 \leq \beta \leq 0.2$ (see Fig. 8.3). The interaction domain between the two particles that share the contact point c is a cylinder of radius equal to the radius of the smaller of the two particles in contact. The circular section at point c of radius r_c is the contact interface between particles i and j. This definition of the contact interface and the interaction domain is motivated by the fact that the two interacting particles can have very different radius for an
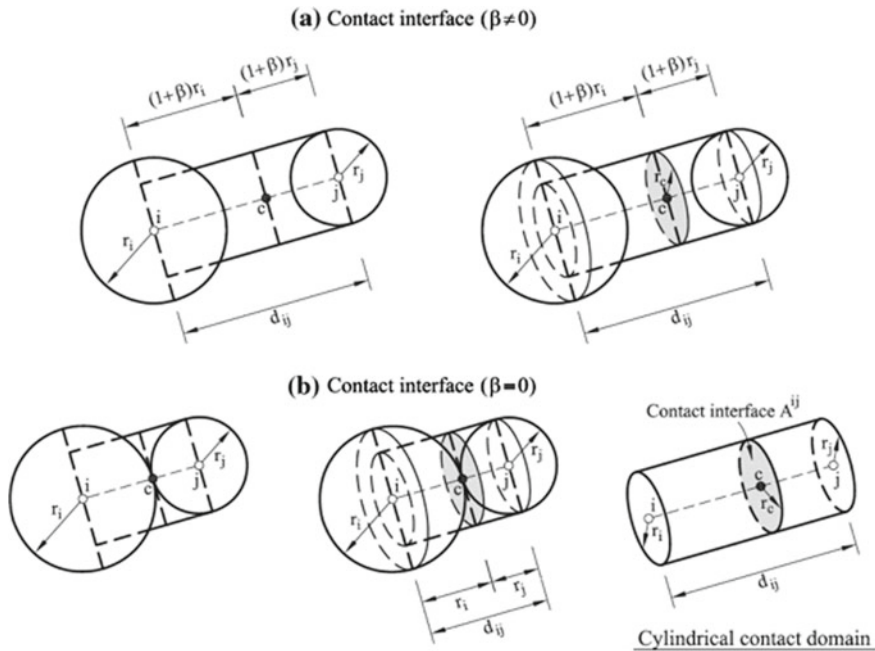
Fig. 8.3 Definition of the DEM contact interface

arbitrary distribution of the particle sizes. The contact interface is thus limited by the size of the smaller of the two particles in contact.

The overall mechanical behavior of a material can be reproduced by associating a simple constitutive law to each contact interface. The interaction between spherical (in 3D) or circular (in 2D) particles i and j with radius r_i and r_j, respectively, is defined within an interaction range. This range allows for a certain gap or an overlapping between the particles. Then two particles will interact if:

$$1 - \beta \leq \frac{d_{ij}}{(r_i + r_j)} \leq 1 + \beta \qquad (8.1)$$

where d_{ij} is the distance between the centroids of particles i and j and β is the interaction range parameter.

Decomposition of the Contact Forces

Once contact between a pair of elements has been detected, the forces occurring at the contact point are calculated. The contact between the two interacting spheres can be represented by the contact forces F^{ij} and F^{ji}. F^{ij} can be decomposed into the normal and tangential components, as shown in Fig. 8.4.
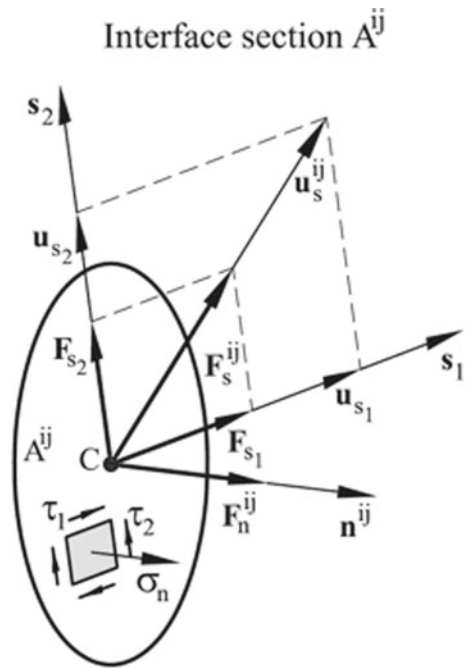
Figure 8.5 shows how the tangential force can be written in terms of the shear direction components.
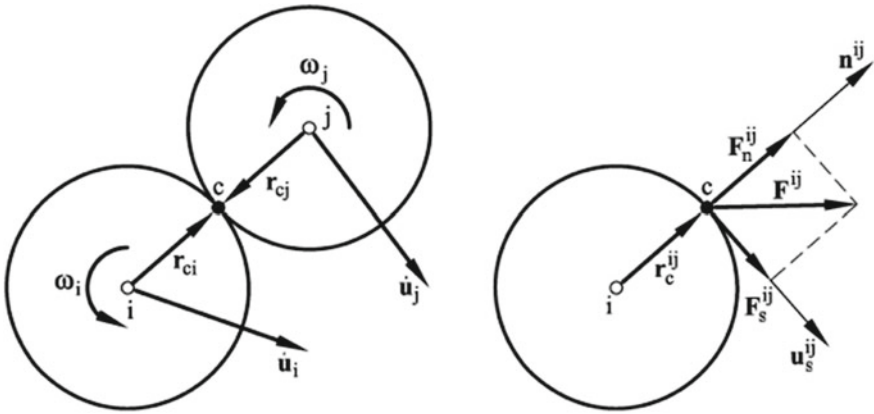
Fig. 8.4 Decomposition of the contact force into its normal and tangential components

Fig. 8.5 Forces and stresses acting on a contact interface section. Definition of normal and shear directions

8.2.1.3   Equations of Motion

The translational and rotational motion of rigid spherical or cylindrical particles is described by means of the standard equations of rigid body dynamics. For the ith particle we have:

$$m_i \ddot{\mathbf{u}}_i = \mathbf{F}_i$$

$$\bar{\bar{\mathbf{I}}}_i \dot{\omega}_i = \mathbf{T}_i$$

(8.2)

where $\mathbf{u}_i$ is the element centroid displacement in a fixed (inertial) coordinate frame, $\dot{\omega}_i$ the angular velocity, m_i the element mass, $\bar{\bar{\mathbf{I}}}_i$ the moment of inertia, $\mathbf{F}_i$ the resultant force and $\mathbf{T}_i$ the resultant moment about the central axes. Vectors $\mathbf{F}_i$ and $\mathbf{T}_i$ are sums of:

- All forces and moments applied to the ith particle due to external loads.
- Contact interactions with neighbouring spheres.
- Forces and moments resulting from external damping.

Equations (8.2) are integrated in time using a simple central difference scheme.

8.2.1.4   The DEM Elastic Constitutive Parameters

This implemented DEM numerical model assumes a proportionality between the normal force at each contact interface and the relative displacement and velocity of the contact point. Like for the shear force, this is assumed to be proportional to the relative sliding motion at the contact point. The proportionality coefficients are estimated starting from the one-dimensional stress-strain relationship for the cylindrical contact domain. For solid materials (such as ice), the existence of a matrix between grains (modelled via a gap distance) prevents in most cases the direct contact between particles. This justifies the selected contact law for the model.

Normal Contact Force Parameters

The normal force F_n^{ij} at the contact interface between particles i and j is obtained as:

$$F_n^{ij} = \sigma_n \bar{A}^{ij}$$

(8.3)

where σ_n is the normal stress at the contact interface and $\bar{A}^{ij}$ is the effective area at the interface. The normal stress is related to the normal strain between the spheres ε_n by a visco-elastic law as:

$$\sigma = E \varepsilon_n + c \dot{\varepsilon}_n$$

(8.4)

where the normal strain and the normal strain rate are defined as:

$$\varepsilon_n = \frac{u_n}{d_{ij}}, \qquad \dot{\varepsilon}_n = \frac{\dot{u}_n}{d_{ij}}$$

(8.5)

Shear Force Parameters

A similar approach is followed for obtaining the relationship between the shear forces and the relative tangential displacements at each contact interface. The shear forces in the s_1 and s_2 directions are given by:

$$F_{s1} = \tau_1 \bar{A}^{ij}, \qquad F_{s2} = \tau_2 \bar{A}^{ij} \tag{8.6}$$

where τ_1 and τ_2 are the shear stresses at the contact interface. These stresses are linearly related to the shear strains and at the interface by:

$$\tau_1 = G\gamma_1, \qquad \tau_2 = G\gamma_2 \tag{8.7}$$

where G is the shear modulus, and a simple definition for the shear strains is given by:

$$\gamma_1 = \frac{u_{s1}}{d_{ij}}, \qquad \gamma_2 = \frac{u_{s2}}{d_{ij}} \tag{8.8}$$

where u_{s1} and u_{s2} are the components in the s_1 and s_2 directions of the relative tangential displacement vector at the contact point.

Novel Computation of the Elastic Forces Between Particles

A new way for computing the contact forces between discrete particles is proposed in (Celigueta et al. [2]). The newly proposed forces model takes into account the surroundings of the contact, not just the contact itself. This brings in the missing terms that provide an accurate approximation to an elastic continuum, and avoids calibration of the DEM parameters for the purely linear elastic range. This novel computational model proposes a way to enrich the spring dash-pot model in such a way that the elastic properties of a continuum can be accurately captured with the DEM. Capturing an accurate elastic response of the continuum is a pre-requisite to capture the formation of cracks. Based on the stress tensor σ^i at the ith contact point, which is typically computed for post-processing the DEM results, the new accurate modelling allows to re-compute the elastic forces between particles. For the normal contact forces:

$$F_n^{ij} = K_n^{ij} u_n^{ij} + A^{ij} \nu (\sigma_{s1}^{ij} + \sigma_{s2}^{ij}) \tag{8.9}$$

and for the shear contact forces:

$$F_{s1}^{ij} = K_s^{ij} u_{s1}^{ij} + G A^{ij} \left(\frac{\partial u_n}{\partial s_1} \right)^{ij}$$

$$F_{s2}^{ij} = K_s^{ij} u_{s2}^{ij} + G A^{ij} \left(\frac{\partial u_n}{\partial s_2} \right)^{ij} \tag{8.10}$$

Note that as stated, the stress tensor is used, which for the ith particle, considered as an sphere, is defined as:

$$\sigma^i = \frac{1}{V_i} \sum_{i=1}^{n^c} l_i \otimes F_i \tag{8.11}$$

where n^c is the number of contacts of the particle, l_i is the vector connecting the center of the particle to the ith contact point, F_i is the force vector at the ith contact point (including normal and tangential components) and V_i is the volume used to average the stresses.

Elasto-Damage Model for Tension and Shear

The DEM model presented in the previous sections have been implemented by CIMNE researchers in the DEMpack software[1] over the last 7 years. However, in order to reproduce the behavior of frictional cohesive materials like ice, several important features have been recently development in the DEMpack model, including unidimensional non-linear elasticity, plasticity and damage laws as well as a specific uncoupled fracture criteria.

In the normal and shear failure model, cohesive bonds at a contact interface are assumed to start breaking when the interface strength is exceeded in the normal direction by the tensile contact force, or in the tangential direction by the shear forces (theory of classical stress mechanics). The uncoupled failure (de-cohesion) criterion for the normal and tangential directions at the contact interface between particles i and j is written as:

$$F_{n_t} \geq \Phi_{n_t}$$
$$F_s \geq \Phi_s \tag{8.12}$$

where Φ_{n_t} and Φ_s are the interface strengths for pure tension and shear-compression conditions, respectively. F_{n_t} is the normal tensile force and F_s is the modulus of the shear force vector. The interface strengths are defined as:

$$\Phi_{n_t} = \sigma_t^f \bar{A}^{ij}$$
$$\Phi_s = \tau^f \bar{A}^{ij} + \mu_1 \left| F_{n_c} \right| \tag{8.13}$$

where σ_t^f and τ^f are the tensile and shear failure stresses, respectively (also called tensile and shear strengths), F_{n_c} is the compressive normal force at the contact interface and μ_1 is a (static) friction parameter. These values are assumed to be an intrinsic property of the material and are determined experimentally. Following tension failure, the constitutive behavior in the shear direction is governed by the standard Coulomb law as:

---

[1]see http://www.cimne.com/dempack/.
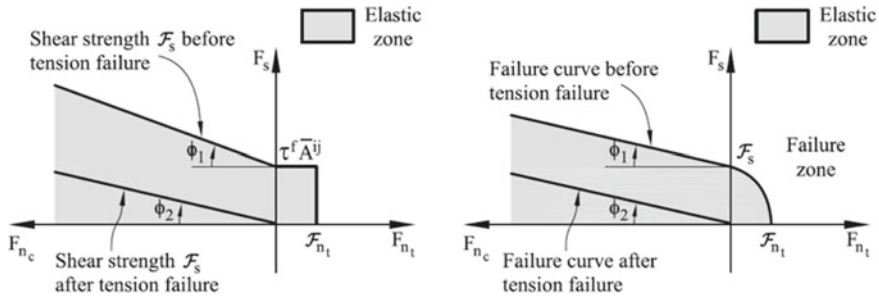
Fig. 8.6 Failure line in terms of normal and shear forces. Uncoupled failure model (left) and coupled failure model (right)
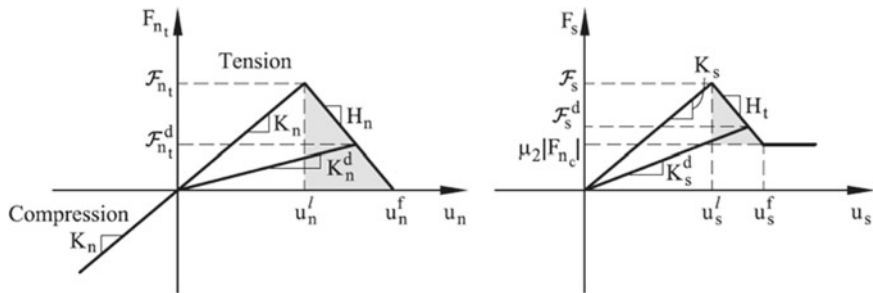
Fig. 8.7 Undamaged and damaged elastic moduli under tension (left) and shear (right) forces

$$F_s = \mu_2 \left| F_{n_c} \right| \frac{u_s}{|u_s|} \tag{8.14}$$

where μ_2 is a dynamic Coulomb friction coefficient. Figure 8.6 shows the graphical representation of the failure criterion described above.

On the one hand, this criterion assumes that the tension and shear forces contribute to the failure of the contact interface in a decoupled manner. On the other hand, shear failure under normal compressive forces follows a failure line that is a function of the shear failure stress, the compression force and the internal friction angle. Indeed, a coupled failure model in the tension-shear zone can also be used, as shown in Fig. 8.6 right.

The model is completed with a damage evolution law. Figure 8.7 shows the evolution of the normal tension force (F_{n_t}) and the shear force F_s at a contact interface until failure, in terms of the relative normal and tangential displacements. The effect of damage in the two constitutive laws is also shown in the figure.

Elastic damage can be accounted for by assuming a softening behavior defined by the softening moduli introduced into the force-displacement relationships in the normal (tensile) and tangential directions, respectively. Damage effects are assumed to start when the failure strength conditions are satisfied. The evolution of the damage

parameters from the value zero to one can be defined in a number of ways using fracture mechanics arguments.

8.2.1.5 DEM Application Example

At the time of writing this document, the validation task of the NICE-SHIP project is not yet completed. Therefore, this section just presents a preliminary application example of the developed methodology. The example is focused on the interaction between an icebreaker ship and an ice floe with different dimensions and thickness. In general lines, we would like to study if with the DEM it is possible to analyse such scenarios and then characterize the results and study the effects on ice loads of the floe size and thickness. Moreover, special interest will be devoted to see if the expected failure pattern of each case is well reproduced.

8.2.1.6 Ship Bow-Ice Interaction

The simulated system consists of a model of a theoretical ship bow advancing with a constant speed towards the modelled ice floe. This analysis includes two elements: the ship bow and the ice floe. The ship bow is considered an structure with imposed motion and discretised with finite elements, whereas the ice floe is composed by an arrangement of bonded particles modeled with the DEM. The characteristics of the ice floe are changed for every simulation. The studied ice floes are grouped according to their dimensions and the characteristic length of the problem (l). For the ship bow, a generic model has been created reproducing the main characteristics of a real icebreaker. It has been considered a stem buttock angle equals to 30º and a draft of 7 m. Figure 8.8 shows different views of it.

In Table 8.1 the computational parameters for the ice material are listed. There are not boundary conditions set to the ice sheets because the aim is to simulate a separate ice floe without or little contacts with its neighbouring ones.
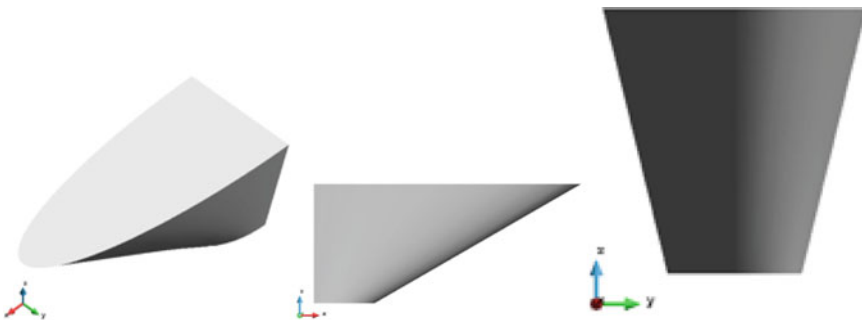
Fig. 8.8 CAD views of the digital ship bow model

Table 8.1 Computational parameters for the ice material

Definitions	Symbols	Values	Units
Type of ice	–	Separate ice floes	–
Ice velocity	ν_i	0	m/s
Density of sea ice	ρ_i	920	kg/m
Young modulus of sea ice	E	3e+9	Pa
Poisson ratio of sea ice	ν	0.33	–
Friction angle of sea ice	ϕ_i	30	°
Ice-ice (static) friction coefficient	μ_{ii}	0.05	–
Ice-structure (static) friction coefficient	μ_{is}	0.25	–
Normal tensile strength	σ_t^f	1.5	MPa
Shear strength	τ^f	1.0	MPa

Table 8.2 Computational parameters for the ship bow structure

Definitions	Symbols	Values	Units
Type of structure	–	Ship bow	–
Structure velocity	ν_s	2.06 (4)	m/s (kn)
Young modulus	E_s	200e+9	Pa
Poisson ratio	ν_s	0.265	–

In Table 8.2 the computational parameters for the ship bow are listed.

Different simulations have been run, for different ratios of the characteristic length of the case (l) and the main dimensions of the ice sheet (L and B). Those cases are classified as:

- Direct floe rotation, $L < l$
- Radial cracking of a finite size wide floe, $l \leq L \leq 2l$
- Radial and transversal cracking of a finite size square floe, $l \leq L \leq 2l$
- Transversal cracking of a finite size long floe, $l \leq B \leq 2l$
- Radial and circumferential cracking of a semi-infinite ice floe $L > 2l$

The characteristic length of the different cases is calculated as:

$$l = \sqrt[4]{\frac{Eh^3}{12(1-\nu^2)\rho_w g}} \tag{8.15}$$

A total of twenty simulations have been carried out, which correspond five to each ice thickness h. The considered ones are 0.5, 1.0, 1.5 and 2.0 m because the first-year sea ice thickness ranges from 0.3 to 2.0 m.

Figure 8.9 shows the evolution at different time steps of the simulation with interaction between the ship bow and an ice floe of 0.5 m thickness and $12 \times 12 \, \text{m}^2$.
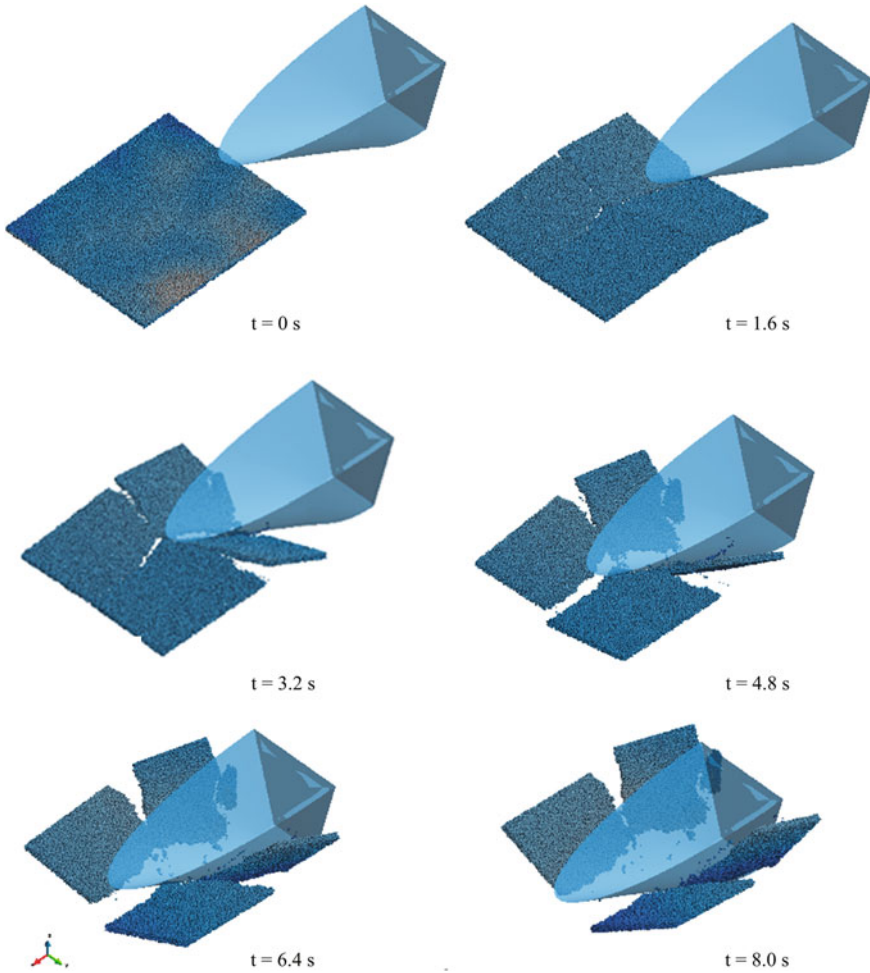
Fig. 8.9 Interaction between ship bow and finite size square ice floe simulated with the DEM. The magnitude of the Y-displacement is presented in different colours

The simulation results highlight how the square ice floe is firstly submerged a bit. This produces that the downward part of the ice floe to be under tension while the upward in compression. Consequently the initiation of a radial crack is produced, from the contact zone and propagated to the end boundary. Since the ice floe is sufficiently long in this case, a transversal crack is also generated more or less in the middle of the floe. Approximately at the simulation time of 1.5 s, the square ice floe is completely separated in four squared parts. They are then are free but subjected to buoyancy effects. Thus, little by little they try to recover the equilibrium state but the ship bow maintains its advancing motion and thus more contacts are produced between the separate parts an the ship hull. Figure 8.10 shows the evolution of the X
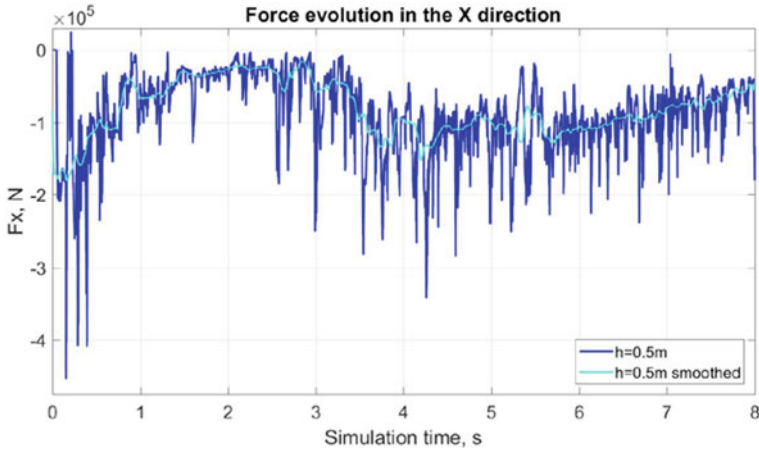
Fig. 8.10   Force evolution in X for the 0.5 m thick ice floe and $12 \times 12\,\text{m}^2$

step 1.5

Contour Fill of DISPLACEMENT, Z-DISPLACEMENT.
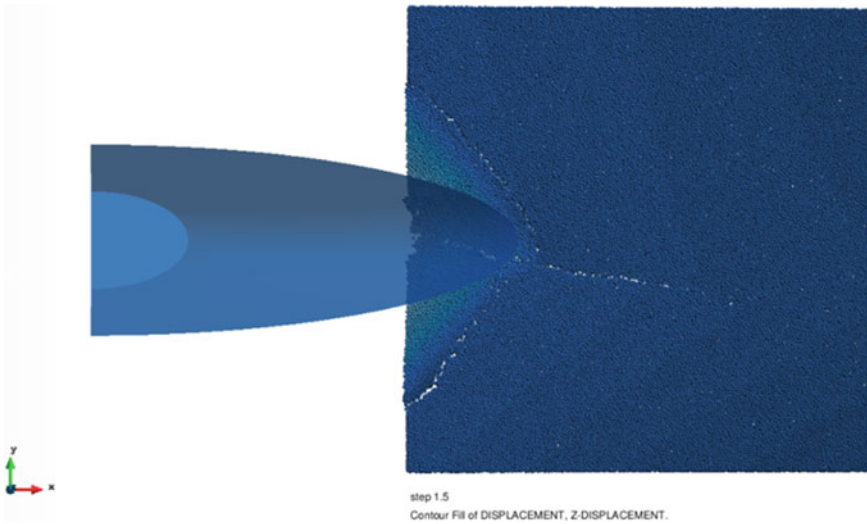
Fig. 8.11   Side view at the simulation case of a semi-infinite square ice sheet (time 1.5 s)

component of the ice load. Since the obtained peaks values are not representative, the data has been smoothed by taking the median over a window of 100 data points. The smoothed values fluctuate between 180.3 kN (maximum) to −16.1 kN (minimum).

Figure 8.11 presents a top view of the Z-displacement for the case of a semi-infinite square ice sheet. It can be seen how the ice sheet fractures both radial and circumferentially. The dimensions are big enough to first create this circumferential crack without affecting the sides of the ice floe.
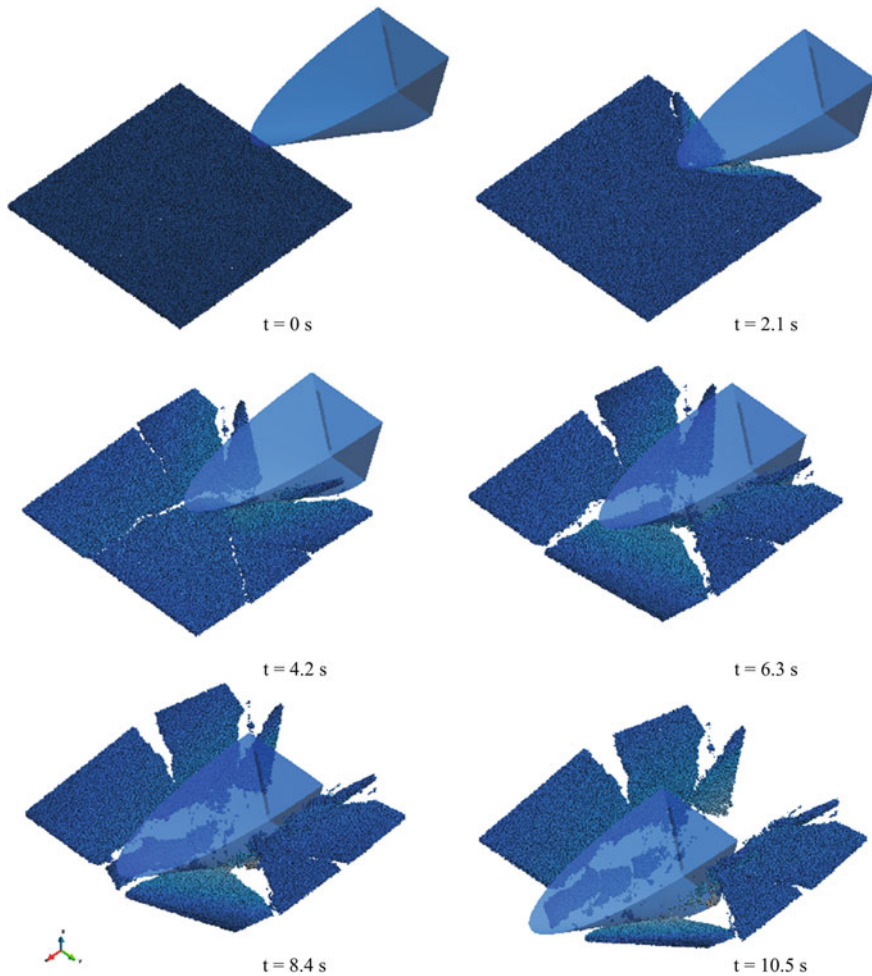
Fig. 8.12 Interaction between ship bow and semi-infinite ice floe simulated with the DEM. The magnitude of the Z-displacement is presented in different colors

Figure 8.12 shows the evolution at different time steps of the simulation with interaction between the ship bow and a semi-infinite ice floe of 0.5 m thickness and an area of $17 \times 17 \, \text{m}^2$.

The simulation results show how the semi-infinite square ice floe firstly fractures creating a set of circumferential cracks. At the same time, a radial crack is initiated and then propagated to the end contour. When the ship bow contacts again with the ice floe, a second set of circumferential cracks appears, but now more difficult to identify because the sides are affected. Looking to the steps at the end of the simulation, any behavior pattern cannot be identified. The already broken pieces of ice are displaced to the side by the ship's hull when it advances.
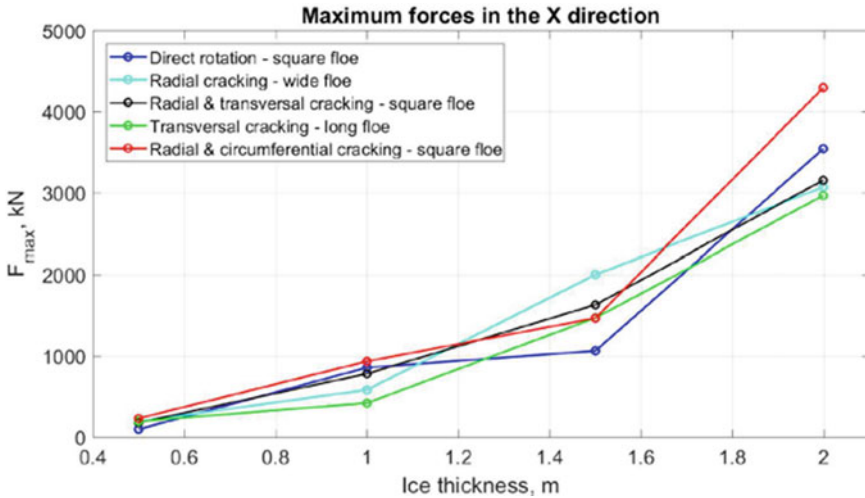
Fig. 8.13 Map compilation of ice loads in the X direction

Finally, Fig. 8.13 shows a summary of the ice loads in the *X* direction calculated in the different analysed cases. For each ice-sheet thickness, the maximum force calculated is plotted. As expected, the trend shows that when ice thickness increases, the ice load does as well.

8.2.2 Scenario 2: Analysis of the Performance of Ships in Brash Ice

8.2.2.1 Introduction to the Semi-Lagrangian Particle Finite Element Method

The Semi-Lagrangian Particle Finite Element Method (SL-PFEM) was presented for the first time in (Nadukandi et al. [22]) and is based on using a Lagrangian method for the convective transport of momentum, along with the Finite Element Method (FEM) to integrate the elliptic part of the momentum equation and the continuity equation. The SL-PFEM can be considered the latest development within the framework called Particle Finite Element Method (PFEM) (Idelsohn et al. [13]). The SL-PFEM contributes to this framework with the semi-Lagrangian formulation based on an explicit integration of the velocity and acceleration along streamlines (X-IVAS (Idelsohn et al. [15])) and with a semi-implicit fractional step scheme (see Fig. 8.14). The semi-Lagrangian (SL) name identifies those schemes that are derived from a Lagrangian formulation of the discrete equations, but solved partially in an Eulerian manner. In our case, particles transporting momentum (velocity) are advanced forward in time following the pathlines described by the velocity field. Then, implicit corrections due to viscosity and flow incompressibility are solved
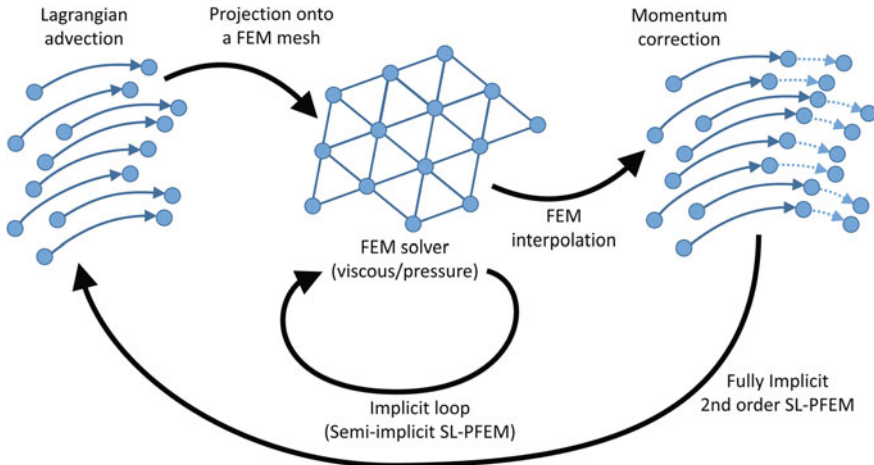
Fig. 8.14 Conceptual description of the SL-PFEM

in a background mesh using the FEM. Finally, the particles' velocity is updated interpolating the implicit corrections at the new particles' positions. Unlike other particle methods, the SL-PFEM does not use material points, but marker points that contains the value of extrinsic variables at a specific time and at the position of the particle. Then particles can be added or removed without affecting extrinsic variables such as mass. One of the main advantages demonstrated by the SL-PFEM is that it is a faster code compared to more traditional computational fluid dynamics methods (Nadukandi et al. [22]). This is due to the possibility of using large time steps without compromising the neither the stability nor the accuracy of the method, achieving up to 10 to 15 times the Courant number. Celledoni et al. [3] showed that the second order SL schemes with Eulerian storage are indeed second order approaches to the standard second order exponential integrators. This connection explains why SL schemes can handle large time steps without damaging the accuracy of the solution.

Figure 8.14 represents the fundamental of the SL-PFEM. The bottom line is to solve the convective transport of momentum moving the particles along the pathlines to the following time step (which requires an accurate prediction of the pathlines). Then the particles' momentum is mapped onto a background mesh, where the momentum is corrected. This correction accounts for the acceleration induced by pressure and viscosity effects. Finally, this correction is interpolated at the particles' position and added to the particles' momentum. The strong point of this method lies on using a Lagrangian scheme for the convective transport, and using the FEM to solve the elliptic part of the Navier Stokes equations. All these results naturally in a stable and accurate numerical scheme.

Below, a brief description of the theoretical basis of the method applied to incompressible flows is presented. Table 8.3 shows the notation used in this section.

On one hand, in the Lagrangian kinematics of the SL-PFEM, the main independent variables are (λ, t), while the main dependent variable is the particles' trajectory,

Table 8.3 Notation used in the introduction to SL-PFEM

$\mathbf{x}$	Spatial coordinates vector
t	Time variable
λ	Particles' label that identifies a fluid particle
$\mathbf{u}(\mathbf{x}, t)$	Fluid velocity at position $\mathbf{x}$ and time t
$\mathbf{u}^h(\mathbf{x}, t)$	Fluid velocity at position $\mathbf{x}$ and time t projected onto the background mesh
$\mathbf{a}(\mathbf{x}, t)$	Fluid acceleration at position $\mathbf{x}$ and time t
$\mathbf{a}^h(\mathbf{x}, t)$	Fluid acceleration at position $\mathbf{x}$ and time t projected onto the background mesh
$p(\mathbf{x}, t)$	Pressure at position $\mathbf{x}$ and time t
$p^h(\mathbf{x}, t)$	Pressure at position $\mathbf{x}$ and time t projected ono the background mesh
$\mathbf{X}(\lambda, t)$	Position of particle λ at time t
$\mathbf{X}^h(\lambda, t)$	Position of particle λ at time t obtained integrating $\mathbf{u}^h$, $\mathbf{a}^h$
$\mathbf{U}(\lambda, t)$	Velocity of particle λ at time t
$\mathbf{U}^h(\lambda, t)$	Discrete velocity of particle λ at time t
$\hat{\mathbf{u}}(\mathbf{x}, t)$	Fluid velocity at position $\mathbf{x}$ and time t obtained by projected the velocity of the particles onto the background mesh
$\mathbf{f}$	External acceleration field
ν	Kinematic viscosity
ρ	Fluid density
$\wp^h$	Projector operator that project the particles' variables onto the background mesh nodes

given by $\mathbf{X}(\lambda, t)$. On the other hand, in the Eulerian kinematics, the independent variables $(\mathbf{x}, t)$, while the main dependent variable is the velocity field $\mathbf{u}(\mathbf{x}, t)$.

An Eulerian description of the incompressible Navier–Stokes equation is:

$$\nabla \cdot u = 0 \tag{8.16}$$

$$\partial_t \mathbf{u} + (\mathbf{u} \cdot \nabla)\mathbf{u} - \nu \Delta \mathbf{u} + \nabla(p/\rho) = \mathbf{f}$$

The fluid acceleration field at $(\mathbf{x}, t)$ is obtained from the momentum as:

$$\mathbf{a} = \partial_t \mathbf{u} + (\mathbf{u} \cdot \nabla)\mathbf{u} = \nu \Delta \mathbf{u} - \nabla\left(\frac{p}{\rho}\right) + \mathbf{f} \tag{8.17}$$

Additionally, the fundamental kinematics equations connect the Eulerian and Lagrangian descriptions as follows:

$$\mathbf{U}(\lambda, \mathbf{t}) : \frac{d\mathbf{X}(\lambda, t)}{dt} = \mathbf{u}(\mathbf{X}(\lambda, t), t)$$

$$\frac{d\mathbf{U}(\lambda, t)}{dt} : \frac{d^2\mathbf{X}(\lambda, t)}{dt^2} = \mathbf{a}(\mathbf{X}(\lambda, t), t) \tag{8.18}$$

The basic idea of the X-IVAS scheme is to update the particles' position within a time step $t^n < t < t^{n+1}$ integrating:

$$\frac{d\mathbf{X}^h(\lambda, t)}{dt} = \mathbf{u^h}(\mathbf{X^h}(\lambda, \mathbf{t}), \mathbf{t}) = \mathbf{A}\mathbf{X^h}(\lambda, \mathbf{t}) + \mathbf{b}$$

$$\frac{d\mathbf{U}^h(\lambda, t)}{dt} = \mathbf{a}^h(\mathbf{X}^h(\lambda, t), t) = \mathbf{C}\mathbf{X}^h(\lambda, t) + \mathbf{d}$$

(8.19)

where $\mathbf{u}^h$ and $\mathbf{a}^h$ are piecewise linear approximations defined on a finite elements mesh. Matrices $\mathbf{A}$ and $\mathbf{C}$, and vectors $\mathbf{b}$ and $\mathbf{d}$, are time dependent and constant within each finite element. Then the particles' trajectories and velocities calculated with the previous equations are $\mathbf{X}^h(\lambda, t)$ and $\mathbf{U}^h(\lambda, t)$ respectively. Integration of Eq. (8.16) with the SL-PFEM is based on the following steps (see Fig. 8.14).

1. The Lagrangian transport is carried out integrating Eqs. (8.6) and (8.7), obtaining $\mathbf{X}^h(\lambda, t^{n+1})$ and $\mathbf{U}^h(\lambda, t^{n+1})$ (see Figure (8.15) left).

$$\mathbf{X}^h(\lambda, t^{n+1}) = \mathbf{X}^h(\lambda, t^n) + \int_{t^n}^{t^{n+1}} \mathbf{u^h}\left(\mathbf{X}^h(\lambda, \tau), t^n\right) d\tau$$

$$\mathbf{U}^{\hat{h}}(\lambda, \mathbf{t^{n+1}}) = \mathbf{U}^h(\lambda, t^n) - \gamma \int_{t^n}^{t^{n+1}} \nabla\left(\frac{p\left(\mathbf{X}^h(\lambda, \tau), t^n\right)}{\rho}\right) d\tau$$

(8.20)

$$+\theta \int_{t^n}^{t^{n+1}} \left(\nu \Delta \mathbf{u}^h\left(\mathbf{X}^h(\lambda, \tau), t^n\right) + \mathbf{f}^h\left(\mathbf{X}^h(\lambda, \tau), t^n\right)\right) d\tau$$

where θ and γ are real values between 0 and 1 depending on the integration scheme used.

2. The transported values of the extrinsic variables are projected onto the FEM mesh (see Fig. 8.15 right):

$$\hat{\mathbf{u}}^h(\mathbf{x}, t^{n+1}) = \wp^h(\hat{\mathbf{U}}^h(\lambda, t^{n+1}))$$

(8.21)

3. The pressure at t^{n+1} on the mesh is obtained solving (8.13)–(8.15):

$$(\Delta p^h(\mathbf{x}, t^{n+1})) = \rho \frac{\nabla \cdot \hat{\mathbf{u}}(x, \mathbf{t^{n+1}})}{\Delta t} + \rho \nabla \cdot (\nu \Delta \mathbf{u}^h(x, t^{n+1})) + \mathbf{f}^h(\mathbf{x}, t^{n+1}))$$

$$-\gamma \Delta p^h(\mathbf{x}, t^n) - \theta \rho \nabla \cdot (\nu \Delta \mathbf{u}^h(\mathbf{x}, t^n) + \mathbf{f}^h(\mathbf{x}, t^n))$$

(8.22)

4. Once the pressure at the end of the time step is obtained the projected. If for instance an explicit Euler scheme is used in time, this correction will be:
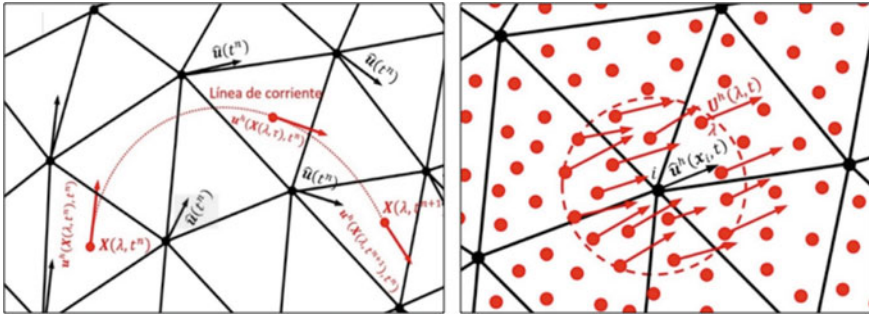
Fig. 8.15 Left. Particle trajectory approximated by streamline using $u^h(x, t)$. Right. Projection of particles' velocity onto node "i"

$$\frac{\mathbf{u}^h(\mathbf{x}, t^{n+1}) - \hat{\mathbf{u}}(\mathbf{x}, t^{n+1})}{\Delta t} = -\nabla \frac{p^h(x, t^{n+1})}{\rho} + (\nu \Delta \mathbf{u}^h(\mathbf{x}, t^{n+1}) + \mathbf{f}^h(\mathbf{x}, t^{n+1}))$$

$$-\gamma \nabla \left(\frac{p^h(\mathbf{x}, t^n)}{\rho} \right) - \theta \left(\nu \Delta \mathbf{u}^h(\mathbf{x}, t^n) + \mathbf{f}^h(\mathbf{x}, t^n) \right)$$

$$(8.23)$$

5. Finally, the particles' velocity is updated increasing the amount $\mathbf{u}^{h,n+1} - \hat{\mathbf{u}}^{h,n+1}$, interpolated at the particles' position:

$$\mathbf{U}^h(\lambda, t^{n+1}) = \hat{\mathbf{U}}^h(\lambda, t^n) + \mathbf{u}^h(\mathbf{X}^h(\lambda, t^{n+1}), t^{n+1}) - \hat{\mathbf{u}}^h(\mathbf{X}^h(\lambda, t^{n+1}), t^{n+1}) \quad (8.24)$$

The SL-PFEM seems like an accurate and efficient alternative to solve complex multiphase flows when compared to others alternatives available nowadays. The method offers a number of advantages, among which we would like to highlight:

- The Lagrangian approach to the convective transport $(\mathbf{u} \cdot \nabla)\mathbf{u}$ of the Navier Stokes equations (8.16) make unnecessary to introduce the typical stabilization terms necessary in convection dominated flows when using other numerical methods.
- The X-IVAS scheme used in the Lagrangian transport step is explicit and unconditionally stable. The first property makes it ideal for an efficient implementation in HPC platforms. And the second is that the size of the time step is not limited by numerical stability but by the precision required. In dominant convection flows it is possible to achieve Courant numbers in the range of 10–15 with good accuracy.
- In dominant convection flows, the pathlines are well approximated by the streamlines. In these cases, the SL-PFEM offer a higher precision.
- Boundary conditions are defined on the mesh boundaries just like in tradition FEM. This confers the method a great flexibility to define complex contours.
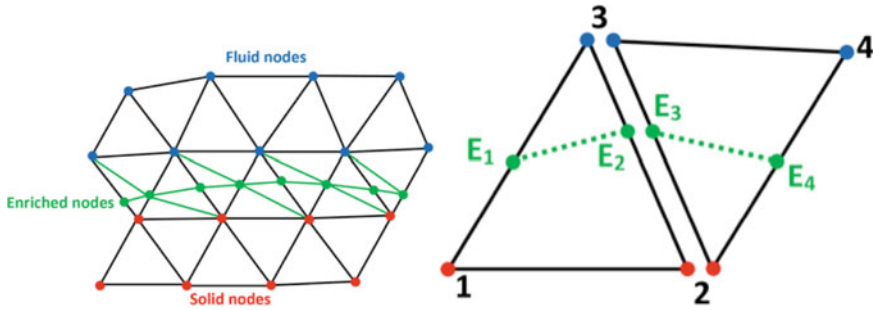
Fig. 8.16 Left: Interface intersection with a FEM mesh and splitting into sub-elements. Right: Enriched nodes generation within an interface element

Further details of the SL-PFEM can be found in (ITTC [1]; Garcia-Espinosa et al. [10, 11]; Idelsohn et al. [13, 14]; Kashteljan et al. [18]; Nadukandi et al. [22]).

8.2.2.2   Modelling Ice Floes as Solid Particles

Solving the ice floes-water interaction requires: to be able to capture the interface corresponding to the solid contours of the ice blocks surrounded by water; solving contacts among rigid bodies (ice blocks and ship); and solving the free surface. The method considered to cope with these interfaces consists of enriching the pressure field in those finite elements cut off by interface (see Fig. 8.16). It is important to highlight that the SL-PFEM allows for naturally enriching the velocity field by just adding new particles within the enriched elements.

For the sake of clarity, the implemented enrichment procedure will be here presented for triangular elements. However, it can be straightforwardly extended to 3D tetrahedral. Figure 8.16 right shows a close up view on two interface elements. It can be observed that for each triangle two enriched nodes are introduced. Then, each intersected element edge will have two enriched nodes, one of each belonging to each triangle sharing that edge. This way each elemental enrichment is local and it will not affect to neighbors' elements, which will allow to solve locally the enriched system avoiding the increase of the number of degrees of freedom in the global system. This will be explained in more detail below.

Once the enriched nodes are introduced, each interface element is divided into three sub-elements. Then each interface element will go from three degrees of freedom to five, and the elemental matrix will be the result of assembling the three sub-elemental matrices. Finally, the global Laplacian matrix $\overline{\overline{\mathbf{K}}}$, corresponding to Eq. (8.22) can be expressed as:

$$\bar{\bar{\mathbf{K}}} = \begin{pmatrix} \bar{\bar{\mathbf{K}}}_f & \bar{\bar{\mathbf{0}}} & \overline{\bar{\mathbf{K}}_{Ef}} \\ \bar{\bar{\mathbf{0}}} & \bar{\bar{\mathbf{K}}}_s & \overline{\bar{\mathbf{K}}_{Es}} \\ \bar{\bar{\mathbf{K}}}^T_{Ef} & \bar{\bar{\mathbf{K}}}^T_{Es} & \bar{\bar{\mathbf{E}}} \end{pmatrix} \begin{pmatrix} \mathbf{P}_f \\ \mathbf{P}_S \\ \mathbf{P}_E \end{pmatrix} = \begin{pmatrix} \mathbf{b}_f \\ \mathbf{b}_S \\ \mathbf{b_E} \end{pmatrix} \tag{8.25}$$

where $\bar{\bar{\mathbf{K}}}_f$ is the Laplacian matrix for the internal fluid nodes, $\bar{\bar{\mathbf{K}}}_s$ is the Laplacian matrix for the internal solid nodes, $\bar{\bar{\mathbf{E}}}$ is the Laplacian matrix for the enriched nodes, and $\bar{\bar{\mathbf{K}}}_{\mathbf{Ef}}$ and $\bar{\bar{\mathbf{K}}}_{\mathbf{Es}}$ are the matrices containing the coupling of the enriched nodes with the fluid and solid nodes respectively.

The advantage of keeping the enrichment local within each interface element is that the matrix $\bar{\bar{\mathbf{E}}}$ becomes:

$$\bar{\bar{\mathbf{E}}} = \begin{pmatrix} \bar{\bar{\mathbf{E}}} & \bar{\bar{\mathbf{0}}} & \cdots & \bar{\bar{\mathbf{0}}} \\ \bar{\bar{\mathbf{0}}} & \bar{\bar{\mathbf{E}}} & \cdots & \bar{\bar{\mathbf{0}}} \\ \vdots & \vdots & \ddots & \vdots \\ \bar{\bar{\mathbf{0}}} & \bar{\bar{\mathbf{0}}} & \cdots & \bar{\bar{\mathbf{E}}} \end{pmatrix} \tag{8.26}$$

Being $\bar{\bar{\mathbf{E_i}}}$ the Laplacian matrix for the enriched nodes within interface element i. Each $\bar{\bar{\mathbf{E_i}}}$ is a 2×2 in 2D problems, and either 3×3 or 4×4 in 3D problems. Since $\bar{\bar{\mathbf{E_i}}}$ are easily invertible, we can calculate:

$$\bar{\bar{\mathbf{E}}}^{-1} = \begin{pmatrix} \bar{\bar{\mathbf{E}}}_1^{-1} & \bar{\bar{\mathbf{0}}} & \cdots & \bar{\bar{\mathbf{0}}} \\ \bar{\bar{\mathbf{0}}} & \bar{\bar{\mathbf{E}}}_2^{-1} & \cdots & \bar{\bar{\mathbf{0}}} \\ \vdots & \vdots & \ddots & \vdots \\ \bar{\bar{\mathbf{0}}} & \bar{\bar{\mathbf{0}}} & \cdots & \bar{\bar{\mathbf{E}}}_n^{-1} \end{pmatrix} \tag{8.27}$$

Using Eq. (8.27) in Eq. (8.25):

$$\mathbf{P}_E = \bar{\bar{\mathbf{E}}}^{-1} \left(\mathbf{b_E} - \bar{\bar{\mathbf{K}}}^{\mathbf{T}}_{Ef} \mathbf{P}_f - \bar{\bar{\mathbf{K}}}^{\mathbf{T}}_{Es} \mathbf{P}_s \right) \tag{8.28}$$

And inserting Eq. (8.28) into Eq. (8.25):

$$\begin{pmatrix} \bar{\bar{\mathbf{K}}}_f - \bar{\bar{\mathbf{K}}}_{Ef} \bar{\bar{\mathbf{E}}}^{-1} \bar{\bar{\mathbf{K}}}^{\mathbf{T}}_{Ef} & -\bar{\bar{\mathbf{K}}}_{Ef} \bar{\bar{\mathbf{E}}}^{-1} \bar{\bar{\mathbf{K}}}^{\mathbf{T}}_{Es} \\ -\bar{\bar{\mathbf{K}}}_{Es} \bar{\bar{\mathbf{E}}}^{-1} \bar{\bar{\mathbf{K}}}^{\mathbf{T}}_{Ef} & \bar{\bar{\mathbf{K}}}_s - \bar{\bar{\mathbf{K}}}_{Es} \bar{\bar{\mathbf{E}}}^{-1} \bar{\bar{\mathbf{K}}}^{\mathbf{T}}_{Es} \end{pmatrix} \begin{pmatrix} \mathbf{P}_f \\ \mathbf{P}_s \end{pmatrix} = \begin{pmatrix} \mathbf{b}_f - \bar{\bar{\mathbf{K}}}_{Ef} \bar{\bar{\mathbf{E}}}^{-1} \mathbf{b}_E \\ \mathbf{b}_s - \bar{\bar{\mathbf{K}}}_{Es} \bar{\bar{\mathbf{E}}}^{-1} \mathbf{b}_E \end{pmatrix}$$
$$\tag{8.29}$$

Equation (8.29) is the new global system of equations for the pressure taking into account the FE enrichment. This system has no extra degrees of freedom thanks to Eq. (8.28), which allows to explicitly write $\mathbf{P}_E$ in terms of $\mathbf{P}_f$ and $\mathbf{P}_s$. This property is a key point from a computational point of view since it avoids to increase the actual

number of degrees of freedom in the global system. Let's remind that increasing the number of degrees of freedom would imply changing the matrix structure with all the computational effort that it carries on.

The iterative process to solve the pressure field is carried out as follows:

$$\mathbf{P}_E^{i+1} = \overline{\overline{\mathbf{E}}}^{-1} \left(\mathbf{b_E^{i+1}} - \overline{\overline{\mathbf{K}}}^{\mathbf{T}}_{\mathbf{Ef}} \mathbf{P}_f^i - \overline{\overline{\mathbf{K}}}^{\mathbf{T}}_{Es} \mathbf{P}_s^i \right) \tag{8.30}$$

$$\begin{pmatrix} \overline{\overline{\mathbf{K}}}_f & \overline{\overline{\mathbf{0}}} \\ \overline{\overline{\mathbf{0}}} & \overline{\overline{\mathbf{K}}}_s \end{pmatrix} \begin{pmatrix} \mathbf{P}_f^{i+1} \\ \mathbf{P_s^{i+1}} \end{pmatrix} = \begin{pmatrix} \mathbf{b}_f^{i+1} - \overline{\overline{\mathbf{K}}}_{Ef} \mathbf{P}_E^i \\ \mathbf{b}_s^{i+1} - \overline{\overline{\mathbf{K}}}_{Es} \mathbf{P}_E^{i+1} \end{pmatrix} \tag{8.31}$$

where the superscript i represent the iteration number. The global pressure matrix remains the same with all the computational advantages that it implies. Let us mention that: on the one hand, collapse of the enriched nodes leads to a loss of continuity in pressure between neighbours interface elements; but on the other hand, this collapse offers a very efficient method, computationally speaking, to cope with discontinuities in the pressure gradient across interfaces.

A similar enrichment scheme is used to solve the free surface interface. The above presented equations are still valid, just considering fluid and gas instead of fluid and solid.

8.2.2.3   SL-PFEM Application Examples

At the time of writing this document, the validation task of the NICE-SHIP project is not yet completed. Therefore, this section just presents a preliminary set of non-validated application examples of the developed methodology.

Patrol Ship Navigating in Ice

In this section, a 2D problem simulating the interaction of a ship with ice blocks is first presented. The main objective is to analyze de interaction of the ice blocks with the ship, and to show the capability of the present approach to simulate a large number of solid bodies immersed in the fluid flow. Three case studies have been simulated, and the particulars for each of them are given in Table 8.4.

Figure 8.17 shows the layout for the three cases under study. Each case contains an array of ice blocks with different sizes, and the mesh refinement is set according to the ice blocks dimensions.

Figure 8.18 shows a snapshot of the ship crossing the swarm of ice floes in the three analysed cases, where the colormaps represent the velocity field.

Figure 8.19 shows the added resistance due to the interaction of the ship with the ice blocks. The units of the resistance are KN per unit of ice thickness. Energy dissipation should be introduce in the collision in order to mimic the behaviour of ice block collisions. However, to do so, ice blocks interactions should be modelled and calibrated based on experimental data.
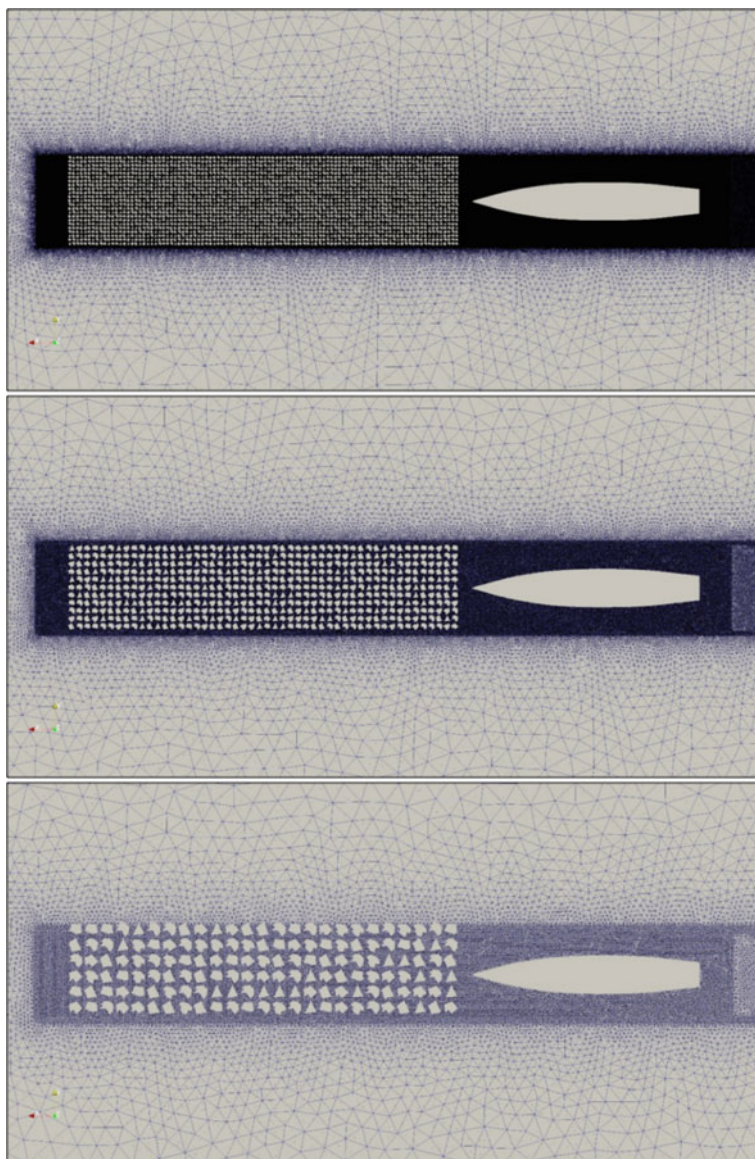
Fig. 8.17 Visualization of Patrol ship, ice blocks, mesh elements and particles. Case 1 (top), Case 2 (middle) and Case 3 (down)
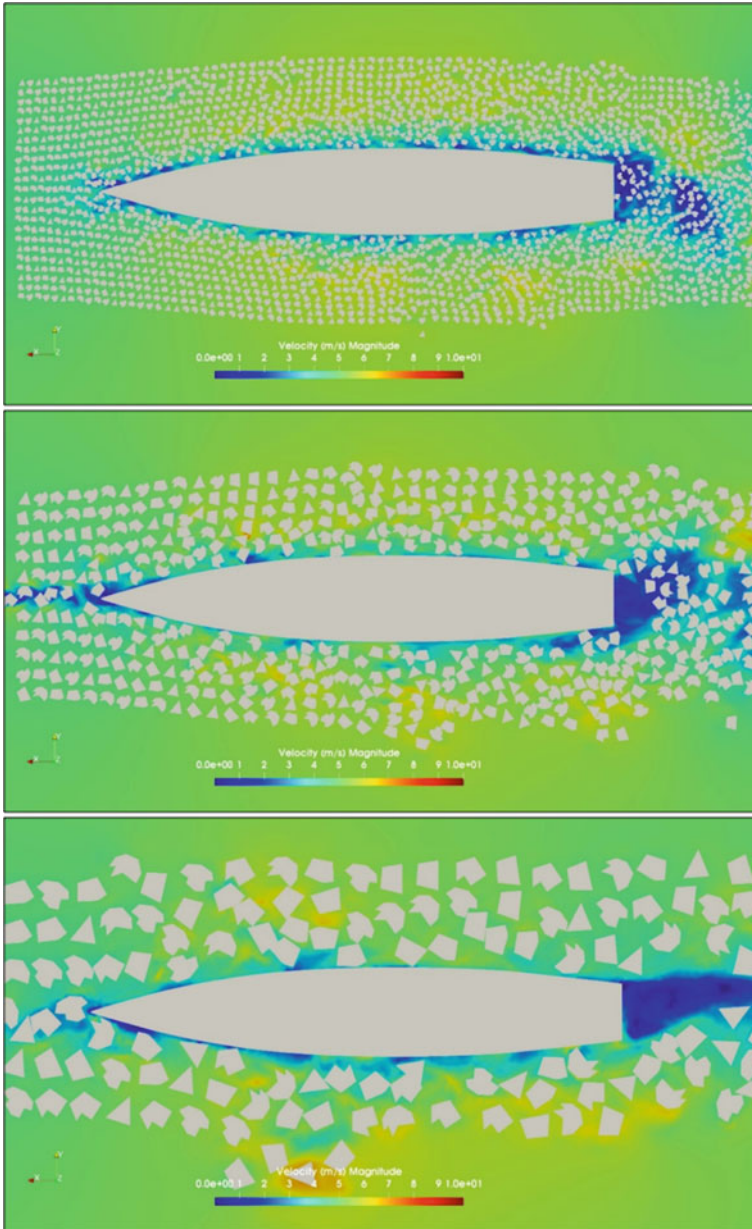
Fig. 8.18 2D Patrol ship crossing a swarm of ice blocks. Case 1 (top), Case 2 (middle) and Case 3 (down)
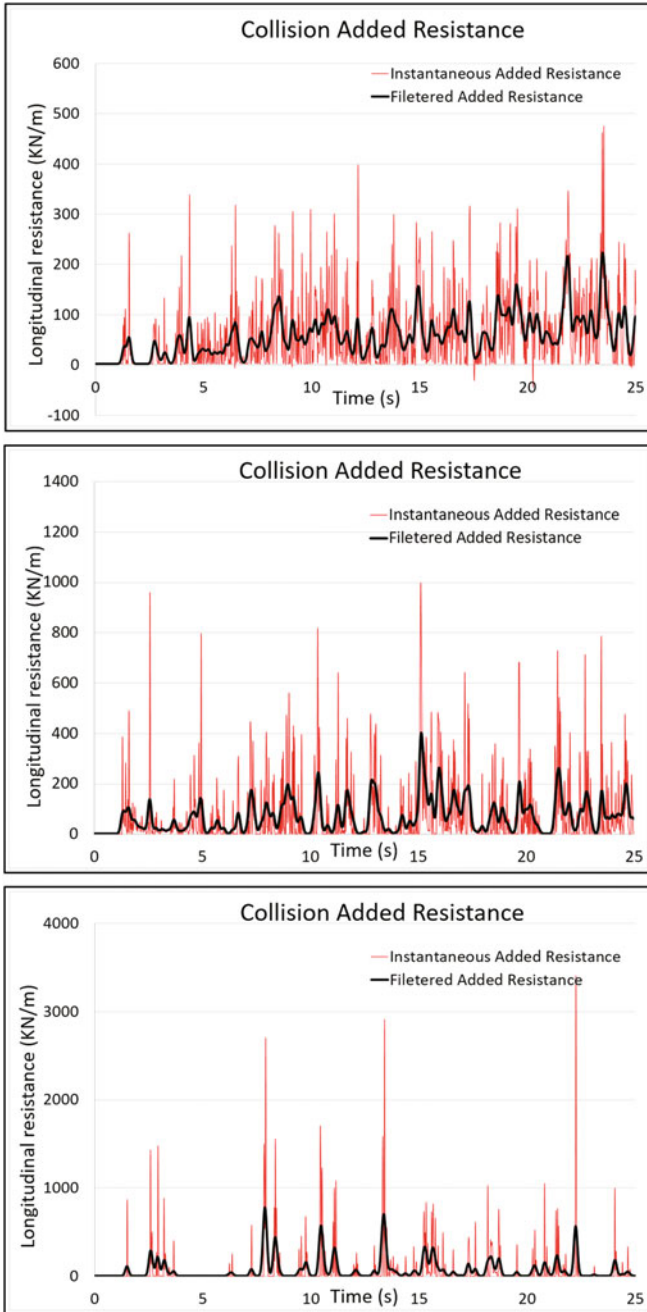
Fig. 8.19 Instantaneous added resistance due to ice block collisions per meter of ice thickness. Case 1 (top), Case 2 (middle) and Case 3 (down)

Table 8.4 Case study particulars

	Particulars	Case 1	Case 2	Case 3
Patrol ship	L_{wl}: Length in waterline	80 m		
	B_{wl}: Beam in waterline	13.64 m		
	V: Velocity	5 m/s		
	Fr: Froude number	0.18		
	Re: Reynolds number	$4 \cdot 10^5$		
Ice	L_{ice}: Characteristic length of ice	1.25 m	2.5 m	5 m
	N_{ice}: Number of ice blocks	2300	550	150
	$\rho_i ce/\rho_w$: Ice-water density ratio	0.92		
Numerical	Δx: Mesh element size	0.175 m	0.35 m	0.7 m
	Δt: Time step	0.025 s		
	$N_{\Delta t}$: Number of time steps	1000		
	N_{elems}: Number of triangle elements	601798	163099	39685
	N_{nodes}: Number of mesh nodes	301389	81794	19979

Table 8.5 3D case study particulars

	Particulars	Case 1
Patrol ship	L_{wl}: Length in waterline	80 m
	B_{wl}: Beam in waterline	13.64 m
	V: Velocity	5 m/s
	Fr: Froude number	0.18
	Re: Reynolds number	$4 \cdot 10^5$
Ice	L_{ice}: Characteristic length of ice	5 m
	t_{ice}: Ice thickness	1 m
	N_{ice}: Number of ice blocks	125
	$\rho_i ce/\rho_w$: Ice-water density ratio	0.92
Numerical	Δx: Mesh element size	0.2 m
	Δt: Time step	0.025 s
	$N_{\Delta t}$: Number of time steps	1000
	N_{elems}: Number of triangle elements	1520443
	N_{nodes}: Number of mesh nodes	277848

Finally, a 3D case analysis is presented. The particulars of this case study are given in Table 8.5, and Fig. 8.20 shows the mesh used.

Finally, Fig. 8.21 shows a snapshot of the ship crossing the swarm of ice blocks, where the colormap represents the velocity field.
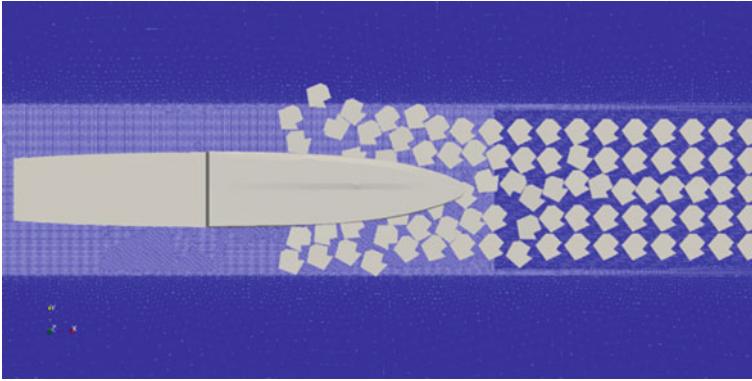
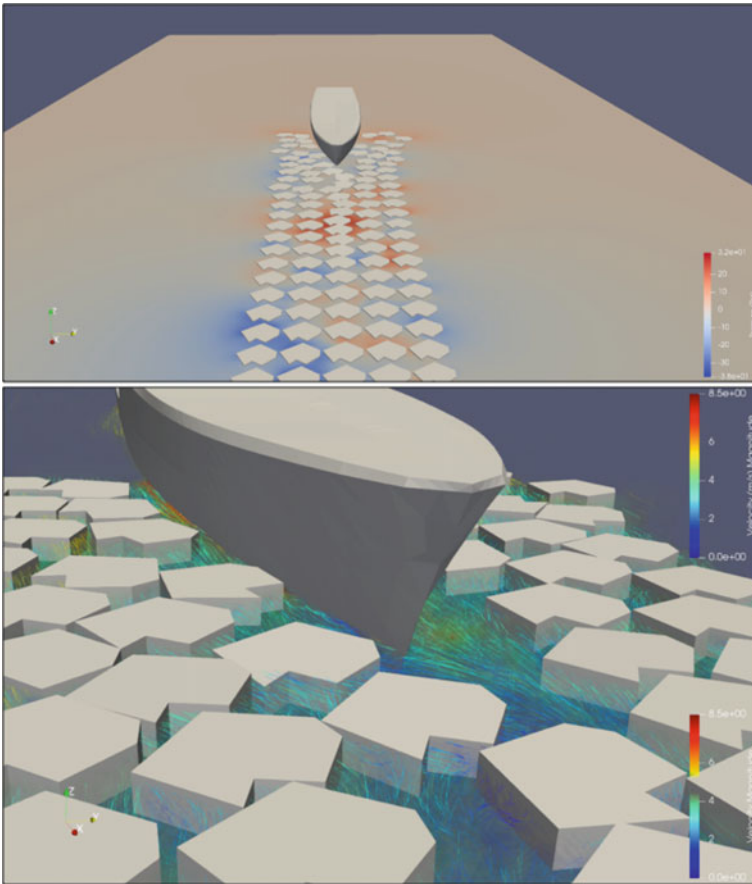**Fig. 8.20** FEM mesh used for the 3D patrol case

Fig. 8.21 3D Patrol ship crossing a swarm of ice blocks

8.3   Conclusions

This document presents the activities carried out to date in the project 'Development of new Lagrangian computational methods for ice-ship interaction problems' (NICE-SHIP). NICE-SHIP is a challenging project aimed at developing a new generation of computational methods, based on the integration of innovative Lagrangian particle-based and finite element procedures for the analysis of the operation of a vessel in an iced sea, taking into account the different possible conditions of the ice.

In order to organize effectively the tasks of the project and focussing on a practical approach, the work of the development team has been focused on the study of two specific scenarios.

The first scenario is the icebreaking of ships in flat surfaces of floating ice of different thicknesses. The goal of this analysis scenario is to validate the constitutive models developed for flat ice analysis, as well as the contact and friction forces models between ship and ice. For this purpose, a constitutive material model in the context of the Discrete Element Method (DEM) has been developed. The model developed to analyse the first scenario will be useful to analyse the icebreaking performance and added resistance of ships in level ice.

The second scenario to be studied is the navigation of ships in brash ice (and broken ice). A FEM semi-Lagrangian fluid-dynamics solver (SL-PFEM) fluid dynamics model has been selected to analyse this scenario. This model will be able to simulate the evolution of the ice around or under the vessel. SL-PFEM solver will be based on the correction of the momentum equation of the fluid-dynamics solver by adding the drag force generated by the ice debris packets. Possible breaking of the larger ice fragments will be ignored in this scenario. This model will be useful to analyse the ice navigation performance of ships and ice-appendages interaction phenomena.

At the time of writing this document, the validation task of the NICE-SHIP project is not yet completed. Therefore, is this document just a set of preliminary application examples of the developed methodology have been presented. However, the results of those cases shows the developed computational techniques as a promising tool to evaluate the loads acting on the structure of a ship navigating in iced-seas and, in particular, to determine the ice resistance of the ship in different ice conditions.

References

1. ITTC-Recommended Procedures and Guidelines (2002). www.ittc.info
2. Celigueta MA, Latorre S, Arrufat F, Onate E (2017) Accurate modelling of the elastic behavior of a continuum with the discrete element method. Comput Mech 60(6):997–1010
3. Celledoni E, Kometa BK, Verdier O (2016) High order semi-Lagrangian methods for the incompressible Navier-Stokes equations. J Sci Comput 66(1):91–115

4. Cho SR, Lee S (2015) A prediction method of ice breaking resistance using a multiple regression analysis. Int J Nav Archit Ocean Eng 7(4):708–719
5. Cho SR, Jeong SY, Lee S (2013) Development of effective model test in pack ice conditions of square-type ice model basin. Ocean Eng 67:35–44
6. Cho S-R, Jeong S-Y, Lee S, Kang, K-J (2014) Development of a prediction formula for ship resistance in level ice. In: ASME 2014 33rd international conference on ocean, offshore and Arctic engineering. American Society of Mechanical Engineers, pp V010T07A024–V010T07A024
7. Corlett ECB, Snaith GR (1964) Some aspects of icebreaker design. Trans R Inst Nav Archit 106(4):389–413
8. Cundall PA (1971) A computer model for simulating progressive, large-scale movement in blocky rock system. In: Proceedings of the international symposium on rock mechanics, 1971
9. Di S, Xue Y, Wang Q, Bai X (2017) Discrete element simulation of ice loads on narrow conical structures. Ocean Eng 146:282–297
10. Garcia-Espinosa J, Camas BS, Cobb JC, Onate E, Latorre, S, Celigueta, MA (2018) Advances in the simulation of ship navigation in ice
11. Garcia-Espinosa J, Valls A, Onate E (2008) ODDLS: a new unstructured mesh finite element method for the analysis of free surface flow problems. Int J Numer Methods Eng 76(9):1297–1327
12. Hu J, Zhou L (2015) Experimental and numerical study on ice resistance for icebreaking vessels. Int J Nav Archit Ocean Eng 7(3):626–639
13. Idelsohn SR, Onate E, Pin FD (2004) The particle finite element method: a powerful tool to solve incompressible flows with free-surfaces and breaking waves. Int J Numer Methods Eng 61(7):964–989
14. Idelsohn S, Nigro N, Limache A, Onate E (2012) Large time-step explicit integration method for solving problems with dominant convection. Comput Methods Appl Mech Eng 217:168–185
15. Idelsohn SR, Marti J, Becker P, Onate E (2014) Analysis of multifluid flows with large time steps using the particle finite element method. Int J Numer Methods Fluids 75(9):621–644
16. Idelsohn S, Oñate E, Nigro N, Becker P, Gimenez J (2015) Lagrangian versus Eulerian integration errors. Comput Methods Appl Mech Eng 293:191–206
17. Ji S, Di S, Liu S (2015) Analysis of ice load on conical structure with discrete element method. Eng Comput 32(4):1121–1134
18. Kashteljan VI, Poznjak II, Ryblin, AJ (1968) Ice resistance to motion of a ship
19. Kim MC, Lee SK, Lee WJ, Wang JY (2013) Numerical and experimental investigation of the resistance performance of an icebreaking cargo vessel in pack ice conditions. Int J Nav Archit Ocean Eng 5(1):116–131
20. Lewis JW, Edwards Jr RY (1970) Methods for predicting icebreaking and ice resistance characteristics of icebreakers
21. Lu W, Lubbad R, Loset S (2014) Simulating ice-sloping structure interactions with the cohesive element method. J Offshore Mech Arct Eng 136(3):031501
22. Nadukandi P, Servan-Camas B, Becker PA, Garcia-Espinosa J (2017) Seakeeping with the semi-Lagrangian particle finite element method. Comput Part Mech 4(3):321–329
23. Onate E, Garcia J, Idelsohn SR (2004) Ship hydrodynamics (2004) in encyclopedia of computational mechanics, vol 2, ed by Hughes TJR, de Borst R, Stein E
24. Onate E, Zarate F, Miquel J, Santasusana M, Celigueta MA, Arrufat F, Gandikota R, Valiullin K, Ring L (2015) A local constitutive model for the discrete element method. Application to geomaterials and concrete. Comput Part Mech 2(2):139–160
25. Shipyards' and Maritime Equipment Association (SeaEurope) (2018) Market forecast report. https://bit.ly/2HsRKVc
26. Su B, Riska-K, Moan T (2010) A numerical method for the prediction of ship performance in level ice. Cold Reg Sci Technol 60(3):177–188
27. Zhou L, Riska-K. Moan T, Su B (2013) Numerical modeling of ice loads on an icebreaking tanker: comparing simulations with model tests. Old Reg Sci Technol 87:33–46